

Article

Lattice Expansion and Crystallite Size Analyses of NiO-BaCe_{0.54}Zr_{0.36}Y_{0.1}O_{3-δ} Anode Composite for Proton Ceramic Fuel Cells Application

Nurul Waheeda Mazlan¹, Munirah Shafiqah Murat², Chung-Jen Tseng³ , Oskar Hasdinor Hassan⁴ 
and Nafisah Osman^{1,2,*} 

¹ Proton Conducting Fuel Cell Group, Universiti Teknologi MARA, Shah Alam 40450, Selangor, Malaysia

² Faculty of Applied Sciences, Universiti Teknologi MARA, Arau 02600, Perlis, Malaysia

³ Center for Energy Research, National Central University, No. 300, Zhongda Rd., Zhongli District, Taoyuan City 320317, Taiwan

⁴ Institute of Science, Universiti Teknologi MARA, Shah Alam 40450, Selangor, Malaysia

* Correspondence: fisha@uitm.edu.my; Tel.: +604-9882272

Abstract: This study reports on the structure analyses of NiO-BCZY (BCZY = BaCe_{0.54}Zr_{0.36}Y_{0.1}O_{3-δ}) anode composite materials with the ratio of 50:50 for proton ceramic fuel cells (PCFCs) application. A product of sintered NiO-BCZY was developed to understand the structural properties of the anode materials. The objectives of this work were (a) to investigate the lattice expansion of the anode by using a high-temperature XRD (HT-XRD) from 400–700 °C; and (b) to calculate the crystallite size of the sample by using Scherrer's and Williamson Hall's methods. The results obtained from the HT-XRD revealed that the diffraction peaks of NiO and BCZY are matched with the cubic phase perovskite structure. For example at T = 400 °C, the lattice parameter of NiO is a = 4.2004 Å and BCZY is a = 4.3331 Å. The observation also showed that the lattice expansion increased with the temperature. Furthermore, analyses of the Scherrer and Williamson Hall methods, respectively, showed that the crystallite size is strongly correlated with the lattice expansion, which proved that the crystallite size increased as the operating temperature increased. The increment of crystallite size over the operating temperature contributed to the increment of conductivity values of the single cell.

Keywords: lattice expansion; crystallite size; NiO-BCZY; anode composite; conductivity; power density



Citation: Mazlan, N.W.; Murat, M.S.; Tseng, C.-J.; Hassan, O.H.; Osman, N. Lattice Expansion and Crystallite Size Analyses of NiO-BaCe_{0.54}Zr_{0.36}Y_{0.1}O_{3-δ} Anode Composite for Proton Ceramic Fuel Cells Application. *Energies* **2022**, *15*, 8520. <https://doi.org/10.3390/en15228520>

Academic Editor:
George Avgouropoulos

Received: 29 September 2022

Accepted: 11 November 2022

Published: 14 November 2022

Publisher's Note: MDPI stays neutral with regard to jurisdictional claims in published maps and institutional affiliations.



Copyright: © 2022 by the authors. Licensee MDPI, Basel, Switzerland. This article is an open access article distributed under the terms and conditions of the Creative Commons Attribution (CC BY) license (<https://creativecommons.org/licenses/by/4.0/>).

1. Introduction

Fuel cells are one of the great sustainable energies which use electrochemical devices that convert chemical energy directly into electrical energy at high efficiency due to the lack of the Carnot constraint of the standard energy conversion chain. One type of fuel cell is a solid oxide fuel cell (SOFC) which comprises oxygen ion (O²⁻)-SOFC and hydrogen ion (H⁺)-SOFC. The H⁺-SOFC, also known as PCFC (proton ceramic fuel cell), is one of the best solutions to operate at intermediate temperatures in the range of 500–800 °C [1–3]. In this operating temperature regime, the components of PCFC, namely, electrode (anode and cathode) and electrolyte materials, are affected by the thermal heat. The changes in size and shape of the materials due to the heat treatment and heating profiles become significant problems, particularly on the anode side which is frequently made of metal and ceramic (cermet) [4–6].

It is important to accurately estimate the structure (for example the crystallite size) of anode cermet as a function of temperature because it influences the characteristics of polycrystalline materials. One of the widely used polycrystalline materials as an anode composite for PCFC is NiO-BaCe_{0.54}Zr_{0.36}Y_{0.1}O_{3-δ} (BCZY) [7–10]. Nickel is used in the

composite anode because it has high catalytic properties for hydrogen oxidation [11]. Furthermore, the use of the composite anode enhances thermal compatibility, reduces interface resistance and lengthens the triple-phase boundary (TPB) [12,13]. In terms of NiO:BCZY composition, it has been reported that more than 40% nickel content can effectively improve electrochemical performance [14,15]. Several studies have discovered that some problems occur, such as fracture formation caused by thermal mismatch between anode layers [16,17]. Hence, data on anode crystallite size are very useful and significant to ensure that the electrolyte component has close TEC under the desired working conditions [18–21].

Most studies have showed a linear relationship between the size of the materials' crystallites and the annealing temperature [22,23]. On the other hand, correlations between the crystallite size of NiO-BCZY anode composite at working temperatures of PCFC are still small in number. Thus, in this work, Scherrer's and Williamson Hall's methods were adopted to calculate the crystallite size of NiO-BCZY that has undergone operating temperatures from 400–700 °C. Williamson Hall's method (W-H method) is more relevant and accurate than Scherrer's method as the lattice strain, lattice stress, and also energy density is taken into account in the calculation [24,25].

In terms of electrical performance of the anode material, research done by Rhidwan et al., showed that crystallite size was inversely proportional to the grain resistance [26]. At 750 °C, the crystallite size of electrolyte bismuth-based materials showed that an almost linear relationship to conductivity can be observed [27]. Thus, the effect of lattice expansion and crystallite size trends on the electrochemical performance, such as conductivity and power density of NiO-BCZY, were also identified in this study.

2. Materials and Methods

Firstly, to prepare the anode composite powder, the raw material of barium nitrate ($\text{Ba}(\text{NO}_3)_2$), cerium (III) nitrate hexahydrate ($\text{Ce}(\text{NO}_3)_3 \cdot 6\text{H}_2\text{O}$), zirconyl (IV) nitrate hydrate ($\text{Zr}(\text{NO}_3)_2 \cdot \text{O} \cdot \text{xH}_2\text{O}$), yttrium (III) nitrate hexahydrate ($\text{Y}(\text{NO}_3)_3 \cdot 5\text{H}_2\text{O}$) were dissolved in deionized water. Nickel (II) nitrate ($\text{Ni}(\text{NO}_3)_2$) and citric acid (CA) were added to the solution, and its pH was adjusted to 7 by using ammonia hydroxide. Next, the mixture was heated at 120 °C overnight and dried at 325 °C for about 2 h. The dried powder was ground and calcined at 1100 °C for 10 h and then pressed at the pressure of 5 MPa for about 1 min to produce a circular pellet. The obtained pellet was sintered at 1400 °C for 6 h.

The sintered pellet was ground using a mechanical grinder to a powder form before being subjected to the high-temperature X-ray diffraction (HT-XRD) from 400 to 700 °C. The Rietveld refinement technique was utilized by using commercial software of Highscore Plus to calculate the lattice expansion at operating temperatures. After refinement, the material structures were observed through visual for electronic and structural analysis (VESTA). Furthermore, the isolated and selected high-intensity peaks that correlate to a larger diffraction angle were chosen to determine the crystallite size using Scherrer's method and several Williamson Hall plot models. These two methods give an extensive range of crystallite sizes.

For Scherrer's method, the crystallite size of the sample (D) was calculated using Equation (1):

$$D = \frac{k\lambda}{\beta_{hkl} \cos \theta_{hkl}} \quad (1)$$

where Scherrer's constant (k) = 0.9, wavelength (λ) = 0.154056 nm for Cu- K_α radiation, θ_{hkl} is Bragg diffraction angle and β_{hkl} is the broadening of the hkl diffraction peak measured at half of its maximum intensity in radians.

On the other hand, the Williamson Hall's method is utilized to predict a more accurate calculation of crystallite size by using three models: uniform deformation model (UDM);

uniform stress model (USDM); and energy density model (UEDM) using Equation (2), Equation (3) and Equation (4), respectively.

$$\beta_{hkl} = \left(\frac{k\lambda}{D} \right) + 4\epsilon \sin \theta \quad (2)$$

$$\beta_{hkl} \cos \theta = \left(\frac{k\lambda}{D} \right) + 4\sigma \frac{\sin \theta}{E_{hkl}} \quad (3)$$

$$\beta_{hkl} \cos \theta = \left(\frac{k\lambda}{D} \right) + 4 \sin \theta \left(\frac{2u}{E_{hkl}} \right)^{\frac{1}{2}} \quad (4)$$

where E_{hkl} is the young modulus for the cubic crystal.

To further characterize the electrochemical properties of NiO-BCZY anode composite, the impedance measurement and I-V characteristics were carried out. The anode composite was fabricated as an anode substrate of PCFC single cell. The substrate was coupled with cathode and electrolyte materials with configuration of anode (substrate) | electrolyte (thin film) | cathode (thin film). The in-house developed of BCZY and LSCF-BCZY (LSCF = $\text{La}_{0.6}\text{Sr}_{0.4}\text{Co}_{0.2}\text{Fe}_{0.8}\text{O}_{3-\delta}$)-BCZY were employed as electrolyte and composite cathode, respectively [28,29]. The fabricated single cell of NiO-BCZY | BCZY | LSCF-BCZY following the previously reported procedure [30] was placed at the sample holder of custom-made conductivity station for the conductivity and power density measurements. The measurement was done using electrochemical impedance spectroscopy (EIS) ZIVE SP2 Electrochemical Workstation (ZIVELAB WonATech) in the temperature ranging from 500 to 700 °C under hydrogen fuel at anode side and stagnant air at cathode side. Impedance spectrum of the cell was analyzed using ZIVE[®] Smart Manager[™] software and I-V polarization curve was plotted for power density assessment.

3. Results

3.1. XRD Pattern

Figure 1 shows the final diffraction pattern of high-temperature XRD for the fine NiO-BCZY anode composite from 400–700 °C. A finely ground powder is needed to achieve an excellent signal-to-noise ratio (SNR) and avoid fluctuation intensity. Both factors will reduce the preferred orientation and thus avoid spottiness and inconsistency analyses [31]. After allowing the pattern shift peaks, all main peaks in the XRD pattern matched with the Joint Committee of Powder Diffraction Standards (JCPDS) file number for NiO is 01-078-0423 and BCZY is 01-089-2485. The respective JCPDS number of NiO and BCZY used was matched with most of the recent papers reported [32–34]. However, a secondary phase of cerium oxide, CeO (JCPDS no.: 00-0040-0593) was also detected in the spectrum as reported by [35]. The presence of this secondary phase will lead to the non-homogenous formation of NiO-BCZY anode composite as a result of partial decomposition of the pre-prepared BCZY phase [36] due to the incomplete reaction between NiO and the ceramic part.

Figure 2 shows the peaks of BCZY at $2\theta = \pm 29.2$ and NiO at $2\theta = \pm 43.1$ is shifted to the low angle of 2θ (left side) indicating that the lattice parameter increased as the temperature raised to 700 °C. This trend was also reported by Sultan et al. [37] on thermal expansion of semiconductor material. The authors explained a diffuse scattering phenomenon that caused by thermal expansion will reduced the intensity in the Bragg positions. The values of lattice parameter for BCZY and NiO at the temperature of 400 to 700 °C are presented in Table 1. The increase in value shows that the lattice went through thermal expansion while heated [38,39]. The value for the goodness of fit (GOF) obtained was in the range of 0.82 to 3.48. The low number of GOFs signifies that the XRD data was effectively refined. Figure 3 shows the result of refinement for Rietveld analysis of XRD pattern and the cubic structure of NiO-BCZY anode composite that has been observed using VESTA software.

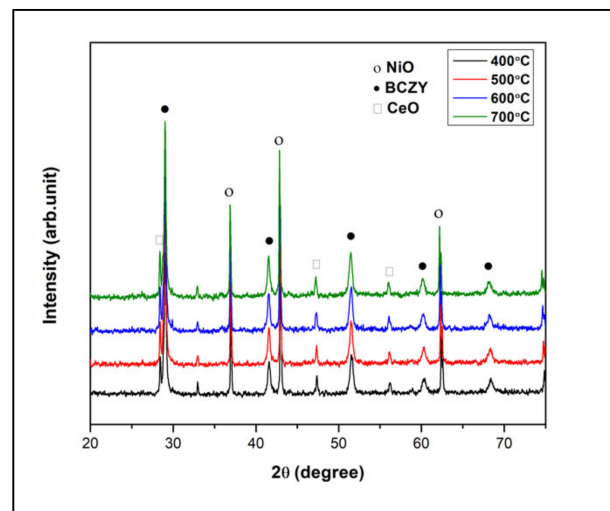


Figure 1. XRD pattern of NiO-BCZY anode composite at four different temperatures (400 to 700 °C).

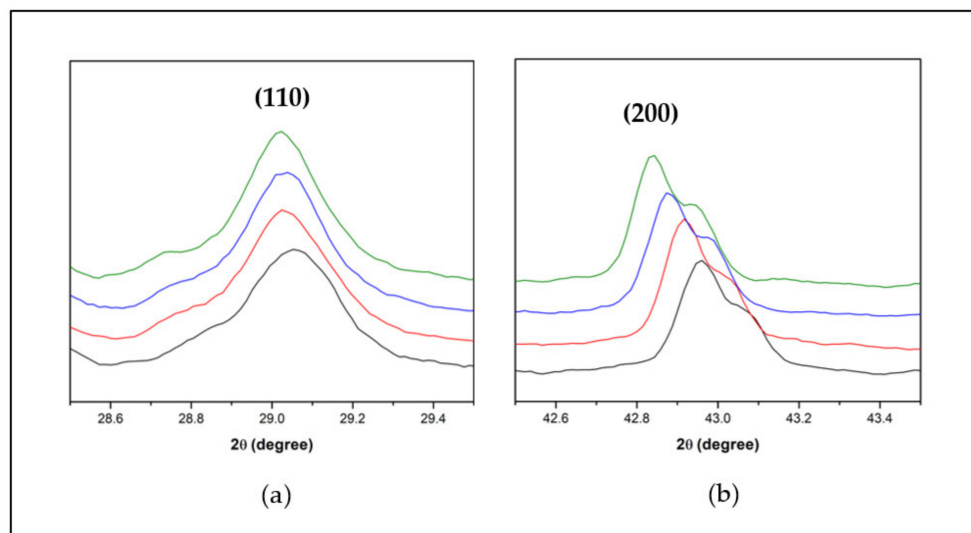


Figure 2. Enlargement of: (a) BCZY peak at (110); and (b) NiO peak at (200) showed that the peaks shift to the left side due to the lattice expansion.

Table 1. The Lattice parameter of NiO and BCZY at temperatures of 400 to 700 °C.

Temp. (°C)	Lattice Parameter, a (Å)	
	NiO	BCZY
400	4.2004	4.3331
500	4.2064	4.3400
600	4.2115	4.3433
700	4.2152	4.3462

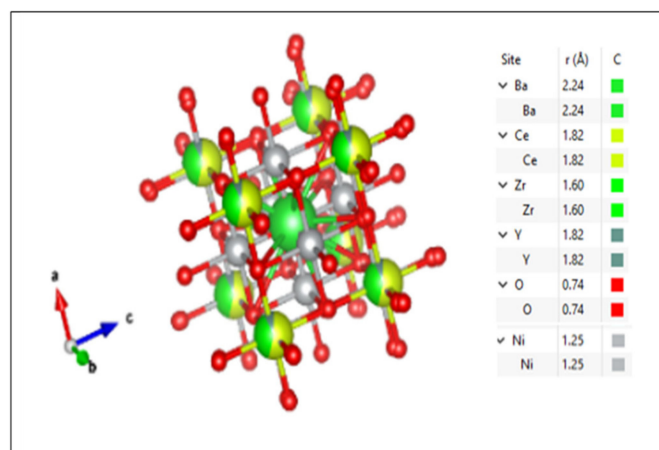


Figure 3. The crystal structure of NiO-BCZY.

3.2. Crystallite Size

The result of crystallite size (D) calculated using Scherrer's method and crystallite size (D), lattice strain (ϵ), deformation stress (σ), and density of energy (U) calculated using, UDM, USDM, and UDEDM models are summarized in Table 2 for NiO and Table 3 for BCZY. The crystallite size of NiO is larger in Scherrer's method as compared to the W-H method which is in contrast with the crystallite size of BCZY. Both methods are similar in terms of dependency on the diffraction angle, θ but can be distinguished as explained in Equations (1)–(4) (Scherrer's is $1/\cos \theta$ dependent and W-H is $\tan \theta$ dependent). Thus, due to different θ positions of respective NiO and BCZY, it will affect the crystallite size and strain broadening data [40]. In addition, the same reason was also explained by Ilyas et al. [41] with the additional factor that contributes to the size and strain such as the widening of the diffraction peak, β . Theoretically, the broadening of the diffraction peak, β is inversely proportional to crystallite size, D [42]. Overall, the average crystallite size showed positive increments as temperature increased due to crystal lattice dilation [37].

Table 2. Summary of crystallite size (D), lattice strain (ϵ), deformation stress (σ) and energy density (U) calculated using a different model for NiO at temperatures of 400 °C to 700 °C.

NiO										
Temp, (°C)	Scherrer Method	Williamson-Hall Method								
		UDM			USDM			UEDDM		
		D (nm)	D (nm)	ϵ ($\times 10^{-3}$)	D (nm)	ϵ ($\times 10^{-3}$)	σ	D (nm)	ϵ ($\times 10^{-3}$)	σ
400	48.71	33.37	12.00	33.37	0.19	28.53	33.37	1.22	186.20	11.32
500	48.79	34.98	11.00	34.98	0.77	118.04	34.98	1.07	163.80	8.76
600	49.01	36.48	8.90	35.15	0.18	28.04	35.32	1.19	183.00	10.94
700	49.34	38.01	8.60	35.32	0.18	27.47	34.65	1.17	179.40	10.51

In addition, the lattice strain is specified as a lattice expansion or contraction due to changes in crystallite size that come from the modification of atomic arrangement [43]. Since strain can be obtained through a slope of the linear fit to the data, a positive slope of lattice strain is attributed to the lattice expansion [44] as shown in Figure 4. Ideal data for the strain were supposed to be decreased as temperature increased as lattice expansion was taken into account; however, due to poor techniques of fitting data, inconsistent results were achieved. The same inconsistent observation was also reported by Yusoff et al. [45].

Table 3. Summary of crystallite size (D), lattice strain (ϵ), deformation stress (σ) and energy density (U) calculated using a different model for BCZY at temperatures of 400 °C to 700 °C.

$\text{BaCe}_{0.54}\text{Zr}_{0.36}\text{Y}_{0.1}\text{O}_{3-\delta}$										
Temp, (°C)	Scherrer Method	Williamson-Hall Method								
		UDM			USDM			UDEDM		
		D (nm)	D (nm)	ϵ ($\times 10^{-3}$)	D (nm)	ϵ ($\times 10^{-3}$)	σ	D (nm)	ϵ ($\times 10^{-3}$)	σ
400	30.91	109.71	3.09	109.71	3.09	472.97	109.71	3.09	472.90	73.01
500	31.62	132.86	5.07	132.85	5.07	777.38	132.85	5.07	777.30	197.20
600	34.31	135.34	4.88	135.34	4.88	746.83	135.34	4.88	746.80	182.00
700	41.82	169.18	4.18	169.18	4.18	639.60	169.18	4.18	639.50	133.50

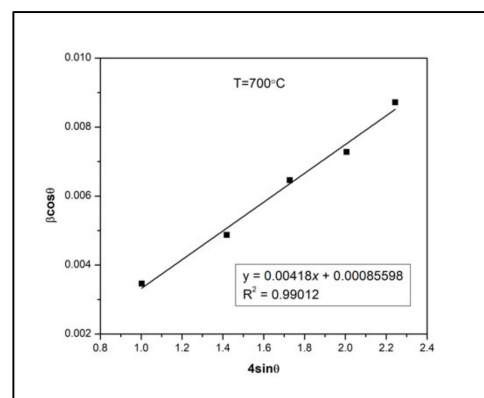


Figure 4. A positive slope of lattice strain for BCZY.

3.3. Electrochemical Measurement

A study on electrical anode performance of NiO-BCZY pellet has been reported elsewhere [46]. Hence, as a continuity work, a single cell was fabricated with a configuration anode | electrolyte | cathode: NiO-BCZY | BCZY | LSCF-BCZY to intensively evaluate the effect of lattice expansion and crystallite size of anode materials on the electrochemical performance. Figure 5 shows a typical Nyquist plot of NiO-BCZY | BCZY | LSCF-BCZY single cell was measured at 700 °C with an inductance ‘tail’ below the x-axis region and two well-defined arcs. The impedance spectrum was fitted using the equivalent circuit $L_s-R_o-(R_1Q_1)-(R_2Q_2)$ where L_s and R_o correspond to the inductance and ohmic resistance, respectively. R_1 and R_2 indicate the resistance from arc-1 and arc-2 where $R_1 + R_2$ is the polarization resistance, R_p of the cell.

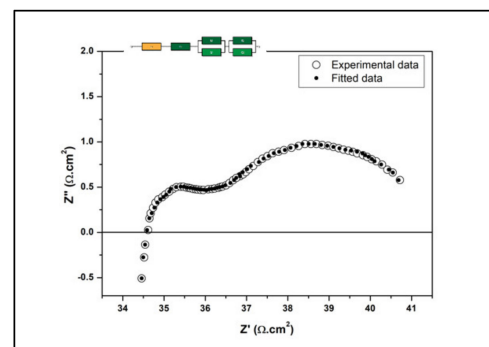


Figure 5. Impedance spectrum of NiO-BCZY | BCZY | LSCF-BCZY single cell at 700 °C under hydrogen/air atmosphere.

Table 4 shows the R_o , R_p and conductivity values of the cell at 500–700 °C. The conductivity increases with increasing temperature demonstrates the involved reactions are temperature dependent and indicates that the corresponding electrochemical reactions are thermally activated processes [47]. The total conductivity of the cell is comparable to a study done by Senari et al. [48] in a similar operation atmosphere.

Table 4. The area specific resistance and total conductivities of single cell at 500–700 °C.

Temperature (°C)	R_o (Ωcm^2)	R_p (Ωcm^2)	Total Conductivity ($\times 10^{-3} \text{ Scm}^{-1}$)
700	34.19	7.90	1.90
600	44.37	8.30	1.52
500	52.45	10.26	1.28

As studied by Hossain et al. [49] the conductivity mechanism was reported as a result of the contribution of ions transportation. For example, the proton transport in crystal lattice of perovskite strongly affect the proton conductivity that occur between the lattices through hopping and reorientation mechanism [50]. Thus, perovskite materials that have large lattice volume tend to form high proton conductivity and vice versa [51]. Greater lattice size promotes more energy to the lattice vibration, which speeds up proton transport and results in better proton conductivity [52].

Shown in Figure 6 is the current-voltage (I-V) and current-power (I-P) plots of the single cell measured when the open circuit voltage (OCV) was stabilized at 700 °C. As compared to our previous study [53], the maximum power density of present findings at 500–700 °C (Table 5) have improved from nW/cm^2 to mW/cm^2 without the need of pore former and material modification. However, the power density of this in-house single cell is noticeably lower than the state-of-art in PCFC technology, particularly NiO-BCZY-based anode composite [9,10,14,46,49]. One of the reasons is due to the ohmic resistance of electrolyte that dominates the cell resistance and influence the OCV of the cell ($\sim 0.21 \text{ V}$ at 700 °C). The small OCV value indicates insufficiently dense electrolyte membrane to prevent gas mixture from anode to cathode, which might explain the overall performance of the cell. Hence, promising fabrication techniques should be taken into consideration for future development [54,55]. On the other hand, it is best to limit or reduce the extreme nickel diffusion from Ni-based cermet anode into barium cerate electrolyte through altering fabrication procedures, for instance, as this tends to result in poor cell performance by lowering the ionic conductivity [56]. Since each research study compares different cell designs, it might be difficult to thoroughly understand the factors that affect the output performance of fuel cells, including fabrication technique, current collector, and gas flow.

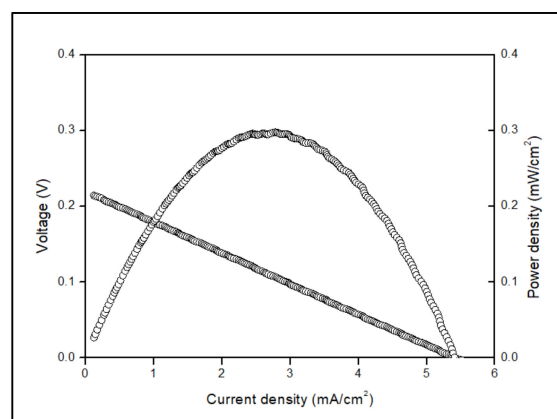


Figure 6. Power density of single cell at 700 °C.

Table 5. Power density value of single cell at 500–700 °C.

Temperature (°C)	Power Density (mW/cm ⁻²)
700	0.48
600	0.30
500	0.18

4. Conclusions

The increase in lattice parameter and unit cell volume indicates that the NiO-BCZY anode composite undergoes lattice expansion at operating temperatures from 400 to 700 °C. The results from Scherrer's method and Williamson-Hall's method showed that the crystallite size increases as the temperature increases. The average value obtained for crystallite size from different models shows that the lattice strain and deformation stress affected the crystallite size. It can be concluded that the Williamson-Hall method gives a more accurate value compared to Scherrer's method. The electrochemical results of the single cell NiO-BCZY | BCZY | LSCF-BCZY exhibited almost linear correlation with the obtained crystallite size data at operating temperatures.

Author Contributions: Writing—original draft preparation, data curation, methodology, N.W.M. and M.S.M.; Conceptualization, writing—review and editing, N.O.; Review, C.-J.T.; Review, Funding acquisition, resources, O.H.H. All authors have read and agreed to the published version of the manuscript.

Funding: This research received UTVSB/CS/P. 20220707006, Petronas (Malaysia).

Data Availability Statement: Not applicable.

Acknowledgments: This work was financially supported by UTVSB/CS/P. 20220707006. The authors thank the Universiti Teknologi MARA and Center for Energy Research of National Central University, Taiwan for the facilities and supports.

Conflicts of Interest: The authors declare no conflict of interest.

References

- Iwahara, H.; Esaka, T.; Uchida, H.; Maeda, N. Proton conduction in sintered oxides and its application to steam electrolysis for hydrogen production. *Solid State Ion.* **1981**, *3*, 359–363. [\[CrossRef\]](#)
- Iwahara, H.; Uchida, H.; Ono, K.; Ogaki, K. Proton Conduction in Sintered Oxides Based on BaCeO₃. *J. Electrochem. Soc.* **1988**, *135*, 529–533. [\[CrossRef\]](#)
- Felseghi, R.A.; Carcadea, E.; Raboaca, M.S.; Trufin, C.N.; Filote, C. Hydrogen fuel cell technology for the sustainable future of stationary applications. *Energies* **2019**, *12*, 4593. [\[CrossRef\]](#)
- Jeong, J.; Azad, A.K.; Schlegel, H.; Kim, B.; Baek, S.W.; Kim, K.; Kang, H.; Kim, J.H. Structural, thermal and electrical conductivity characteristics of Ln_{0.5}Sr_{0.5}Ti_{0.5}Mn_{0.5}O_{3±δ} (Ln: La, Nd and Sm) complex perovskites as anode materials for solid oxide fuel cell. *J. Solid State Chem.* **2015**, *226*, 154–163. [\[CrossRef\]](#)
- Shao, Z.; Tadé, M.O. Anodes for IT-SOFCs. In *Intermediate-Temperature Solid Oxide Fuel Cells*; Springer: Berlin/Heidelberg, Germany, 2016; pp. 127–175. ISBN 9783662529362.
- Lam, N.H.; Smith, R.P.; Le, N.; Thi, C.; Thuy, T.; Tamboli, M.S.; Tamboli, A.M.; Alshehri, S.; Ghoneim, M.M.; Tam, N.; et al. Evaluation of the Structural Deviation of Cu/Cu₂O Nanocomposite Using the X-ray Diffraction Analysis Methods. *Crystals* **2022**, *12*, 566. [\[CrossRef\]](#)
- Shen, C.T.; Lee, Y.H.; Xie, K.; Yen, C.P.; Jhuang, J.W.; Lee, K.R.; Lee, S.W.; Tseng, C.J. Correlation between microstructure and catalytic and mechanical properties during redox cycling for Ni-BCY and Ni-BCZY composites. *Ceram. Int.* **2017**, *43*, S671–S674. [\[CrossRef\]](#)
- Lee, S.; Park, S.; Wee, S.; Baek, H.W.; Shin, D. One-dimensional structured La_{0.6}Sr_{0.4}Co_{0.2}Fe_{0.8}O_{3-δ}—BaCe_{0.5}Zr_{0.35}Y_{0.15}O_{3-δ} composite cathode for protonic ceramic fuel cells. *Solid State Ion.* **2018**, *320*, 347–352. [\[CrossRef\]](#)
- Lee, K.R.; Tseng, C.J.; Jang, S.C.; Lin, J.C.; Wang, K.W.; Chang, J.K.; Chen, T.C.; Lee, S.W. Fabrication of anode-supported thin BCZY electrolyte protonic fuel cells using NiO sintering aid. *Int. J. Hydrogen Energy* **2019**, *44*, 23784–23792. [\[CrossRef\]](#)
- Yoo, Y.; Lim, N. Performance and stability of proton conducting solid oxide fuel cells based on yttrium-doped barium cerate-zirconate thin-film electrolyte. *J. Power Sources* **2013**, *229*, 48–57. [\[CrossRef\]](#)

11. Barros Julião, P.S. A-site cation influences on performance, structure and conductivity of a lanthanide-based perovskite electrode for symmetrical solid oxide fuel cells. *J. Power Sources* **2020**, *450*, 227723. [[CrossRef](#)]
12. Zhu, X.; Qian, C.; Sun, F.; Zhang, L.; Liu, X.; Li, D. Perovskite-type $\text{Nd}_{0.5}\text{Sr}_{0.5}\text{Co}_{0.5}\text{Fe}_{0.5}\text{O}_{3-\delta}$ as a novel cathode material for intermediate-temperature solid oxide fuel cell. *J. Alloys Compd.* **2019**, *802*, 415–421. [[CrossRef](#)]
13. Liu, H.; Akhtar, Z.; Li, P.; Wang, K. Mathematical modeling analysis and optimization of key design parameters of proton-conductive solid oxide fuel cells. *Energies* **2014**, *7*, 173–190. [[CrossRef](#)]
14. Bi, L.; Fabbri, E.; Sun, Z.; Traversa, E. $\text{BaZr}_{0.8}\text{Y}_{0.2}\text{O}_{3-\delta}$ -NiO Composite Anodic Powders for Proton-Conducting SOFCs Prepared by a Combustion Method. *J. Electrochem. Soc.* **2011**, *158*, B797. [[CrossRef](#)]
15. Zunic, M.; Chevallier, L.; Radojkovic, A.; Brankovic, G.; Brankovic, Z.; Di Bartolomeo, E. Influence of the ratio between Ni and $\text{BaCe}_{0.9}\text{Y}_{0.1}\text{O}_{3-\delta}$ on microstructural and electrical properties of proton conducting Ni- $\text{BaCe}_{0.9}\text{Y}_{0.1}\text{O}_{3-\delta}$ anodes. *J. Alloys Compd.* **2011**, *509*, 1157–1162. [[CrossRef](#)]
16. Zakaria, N.H.; Yazid, H.; Osman, N. A Short Review on the Development of Anode Materials for Proton Conducting Fuel Cell. *Solid State Sci. Technol. Lett.* **2018**, *19*, 15–18.
17. Azad, A.K.; Abdalla, A.M.; Afif, A.; Azad, A.; Afroze, S.; Idris, A.C.; Park, J.Y.; Saqib, M.; Radenahmad, N.; Hossain, S.; et al. Improved mechanical strength, proton conductivity and power density in an 'all-protonic' ceramic fuel cell at intermediate temperature. *Sci. Rep.* **2021**, *11*, 19382. [[CrossRef](#)]
18. Løken, A.; Ricote, S.; Wachowski, S. Thermal and Chemical Expansion in Proton Ceramic Electrolytes and Compatible Electrodes. *Crystals* **2018**, *8*, 365. [[CrossRef](#)]
19. Tarancón, A. Strategies for lowering solid oxide fuel cells operating temperature. *Energies* **2009**, *2*, 1130–1150. [[CrossRef](#)]
20. Heydari, F.; Maghsoudipour, A.; Alizadeh, M. Synthesis and evaluation of effective parameters in thermal expansion coefficient of $\text{Ln}_{0.6}\text{Sr}_{0.4}\text{Co}_{0.2}\text{M}_{0.8}\text{O}_{3-\delta}$ ($\text{Ln} = \text{La}, \text{Nd}$ and $\text{M} = \text{Mn}, \text{Fe}$) perovskite oxide. *Bull. Mater. Sci. Indian Acad. Sci.* **2015**, *38*, 1009–1014. [[CrossRef](#)]
21. Osinkin, D.A.; Bronin, D.I.; Beresnev, S.M.; Bogdanovich, N.M. Thermal expansion, gas permeability, and conductivity of Ni-YSZ anodes produced by different techniques. *SOLID STATE Electrochem* **2014**, *18*, 149–156. [[CrossRef](#)]
22. Kibasomba, P.M.; Dhlamini, S.; Maaza, M.; Liu, C.P.; Rashad, M.M.; Rayan, D.A.; Mwakikunga, B.W. Strain and grain size of TiO_2 nanoparticles from TEM, Raman spectroscopy and XRD: The revisiting of the Williamson-Hall plot method. *Results Phys.* **2018**, *9*, 628–635. [[CrossRef](#)]
23. Monshi, A.; Foroughi, M.R.; Monshi, M.R. Modified Scherrer Equation to Estimate More Accurately Nano-Crystallite Size Using XRD. *World J. Nano Sci. Eng.* **2012**, *02*, 154–160. [[CrossRef](#)]
24. Rabiei, M.; Palevicius, A.; Dashti, A.; Nasiri, S.; Monshi, A.; Doustmohammadi, A.; Vilkauskas, A.; Janusas, G. X-ray Diffraction Analysis and Williamson-Hall Method in USDM Model for Estimating More Accurate Values of Stress-Strain of Unit Cell and Super Cells ($2 \times 2 \times 2$) of Hydroxyapatite, Confirmed by Ultrasonic Pulse-Echo Test. *Materials* **2021**, *14*, 2949. [[CrossRef](#)] [[PubMed](#)]
25. Pandya, S.G.; Corbett, J.P.; Jadwisieniczak, W.M.; Kordesch, M.E. Structural characterization and X-ray analysis by Williamson-Hall method for Erbium doped Aluminum Nitride nanoparticles, synthesized using inert gas condensation technique. *Phys. E Low-Dimensional Syst. Nanostruct.* **2016**, *79*, 98–102. [[CrossRef](#)]
26. Rhidwan, I.; Triyono, D.; Laysandra, H. Crystallite size dependence on electrical properties of $\text{LaFeO}_3 \cdot 0.1\text{Fe}_3\text{O}_4$ nanocomposite material. *IOP Conf. Ser. Mater. Sci. Eng.* **2017**, *188*, 012058. [[CrossRef](#)]
27. Ermiş, İ.; Sertkol, M.; Çorumlu, V.; Dagdemir, Y.; Arı, M. Synthesis of $(\text{Bi}_2\text{O}_3)_{0.9-x}(\text{Tb}_4\text{O}_7)_{0.1}(\text{Sm}_2\text{O}_3)_x$ electrolyte for IT-SOFCs. *Synth. React. Inorg. Met. Nano-Metal Chem.* **2016**, *48*, 91–95. [[CrossRef](#)]
28. Osman, N.; Ismail, I.; Samat, A.A.; Md Jani, A.M. Reactivity study of $\text{LaSrCoFeO}_3\text{—Ba}(\text{Ce}, \text{Zr})\text{O}_3$ composite cathode material. *Mater. Sci. Forum* **2016**, *846*, 58–62. [[CrossRef](#)]
29. Ismail, I.; Osman, N.; Md Jani, A.M. Tailoring the microstructure of $\text{La}_{0.6}\text{Sr}_{0.4}\text{Co}_{0.2}\text{Fe}_{0.8}\text{O}_{3-\alpha}$ cathode material: The role of dispersing agent. *J. Sol-Gel Sci. Technol.* **2016**, *80*, 259–266. [[CrossRef](#)]
30. Zakaria, N.H.A.; Affandi, N.S.M.; Zainon, A.N.; Yazid, H.; Osman, N. Electrical Conductivity of Anode Supported NiO-BCZY|BCZY|LSCF-BCZY Button Cell at Intermediate Temperatures. *Solid State Sci. Technol.* **2019**, *27*, 15–21.
31. Bunaciu, A.A.; Udriștioiu, E.G.; Aboul-Enein, H.Y. X-Ray Diffraction: Instrumentation and Applications. *Crit. Rev. Anal. Chem.* **2015**, *45*, 289–299. [[CrossRef](#)]
32. Mazlan, N.W.; Osman, N.; Hassan, O.H. Thermal expansion and lattice parameter of solid electrolyte based on cerate-zirconate ceramics. *AIP Conf. Proc.* **2018**, *2031*, 020014. [[CrossRef](#)]
33. Mazlan, N.W.; Osman, N.; Hassan, O.H.; Mohamed, Z. Lattice Expansion of $\text{BaCe}_{0.54}\text{Zr}_{0.36}\text{Y}_{0.1}\text{O}_{3-\delta}$ Ceramic Electrolyte. *Solid State Phenom.* **2020**, *307*, 149–153. [[CrossRef](#)]
34. Mohd Abd Fatah, A.F.; Rosli, A.Z.; Mohamad, A.A.; Muchtar, A.; Muhammed, M.A.; Hamid, N.A. Electrochemical Evaluation of Nickel Oxide Addition toward Lanthanum Strontium Cobalt Ferrite Cathode for Intermediate Temperature Solid Oxide Fuel Cell (IT-SOFCs). *Energies* **2022**, *15*, 5188. [[CrossRef](#)]
35. Baral, A.K.; Choi, S.; Kim, B.K.; Lee, J.H. Processing and characterizations of a novel proton-conducting $\text{BaCe}_{0.35}\text{Zr}_{0.50}\text{Y}_{0.15}\text{O}_{3-\delta}$ electrolyte and its nickel-based anode composite for anode-supported IT-SOFC. *Mater. Renew. Sustain. Energy* **2014**, *3*, 35. [[CrossRef](#)]

36. Osman, N.; Mazlan, N.W.; Hassan, O.H.; Wan Zulkifli, W.Z.; Mohamed, Z. Phase Analysis of Cerate and Zirconate Ceramics Powder Prepared by Supercritical Ethanol Using High Temperature-High Pressure Batch Wise Reactor System. *Solid State Phenom.* **2020**, *307*, 171–175. [[CrossRef](#)]
37. Sultan, N.M.; Albarody, T.M.B.; Al-jothery, H.K.M.; Abdullah, M.A.; Mohammed, H.G.; Obodo, K.O. Thermal Expansion of 3C-SiC Obtained from In-Situ X-ray Diffraction at High Temperature and First-Principal Calculations. *Materials* **2022**, *15*, 6229. [[CrossRef](#)]
38. Prabhakar Rao, P.A.N. Studies on Structure, Lattice Thermal Expansion and Oxide Ion Conducting Properties of Some Rare Earth Based Zirconate Pyrochlores. Ph.D. Thesis, National Institute for Interdisciplinary Science and (CSIR), Thiruvananthapuram, India, 2012.
39. Hardy, J.S.; Templeton, J.W.; Edwards, D.J.; Lu, Z.; Stevenson, J.W. Lattice expansion of LSCF-6428 cathodes measured by in situ XRD during SOFC operation. *J. Power Sources* **2012**, *198*, 76–82. [[CrossRef](#)]
40. Prabhu, Y.T.; Rao, K.V. X-Ray Analysis by Williamson-Hall and Size-Strain Plot Methods of ZnO Nanoparticles with Fuel Variation. *World J. Nano Sci. Eng.* **2014**, *4*, 21–28. [[CrossRef](#)]
41. Ilyas, S.; Heryanto; Abdullah, B.; Tahir, D. X-ray diffraction analysis of nanocomposite Fe₃O₄/activated carbon by Williamson–Hall and size-strain plot methods. *Nano-Struct. Nano-Objects* **2019**, *20*, 100396. [[CrossRef](#)]
42. Rajesh Kumar, B.; Hymavathi, B. X-ray peak profile analysis of solid-state sintered alumina doped zinc oxide ceramics by Williamson–Hall and size-strain plot methods. *J. Asian Ceram. Soc.* **2017**, *5*, 94–103. [[CrossRef](#)]
43. Kim, H.; Park, N. Importance of tailoring lattice strain in halide perovskite crystals. *NPG Asia Mater.* **2020**, *12*, 78. [[CrossRef](#)]
44. Nath, D.; Singh, F.; Das, R. X-ray diffraction analysis by Williamson-Hall, Halder-Wagner and size-strain plot methods of CdSe nanoparticles- a comparative study. *Mater. Chem. Phys.* **2020**, *239*, 122021. [[CrossRef](#)]
45. Yusoff, A.H.M.; Salimi, M.N.; Jamlos, M.F. Dependence of lattice strain of magnetite nanoparticles on precipitation temperature and pH of solution. *J. Phys. Conf. Ser.* **2017**, *908*, 012065. [[CrossRef](#)]
46. Osman, N.; Senari, S.M.; Md Jani, A.M. Characterization of NiO-BCZY as composite anode prepared by a one-step sol-gel method. *Malays. J. Fundam. Appl. Sci.* **2020**, *16*, 450–452. [[CrossRef](#)]
47. Ismail, I.; Jani, A.M. La_{0.6}Sr_{0.4}Co_{0.2}Fe_{0.8}O_{3-δ} powder: A simple microstructure modification strategy. *J. Sol-Gel Sci. Technol.* **2020**, *94*, 435–447. [[CrossRef](#)]
48. Senari, S.M.; Osman, N.; Jani, A.M.M. Impedance Study on NiO-BaCe_{0.54}Zr_{0.36}Y_{0.10}O_{2.95} Composite Anode for Proton-Conducting Fuel Cell. *J. Phys. Conf. Ser.* **2018**, *1083*, 012026. [[CrossRef](#)]
49. Hossain, S.; Abdalla, A.M.; Zaini, J.H.; Savaniu, C.D.; Irvine, J.T.S.; Azad, A.K. Highly dense and novel proton conducting materials for SOFC electrolyte. *Int. J. Hydrogen Energy* **2017**, *42*, 27308–27322. [[CrossRef](#)]
50. Sata, N.; Matsuta, H.; Akiyama, Y.; Chiba, Y.; Shin, S.; Ishigame, M. Fabrication of proton conducting thin films of SrZrO₃ and SrCeO₃ and their fundamental characterization. *Solid State Ion.* **1997**, *97*, 437–441. [[CrossRef](#)]
51. Norby, T.; Widerøe, M.; Glöckner, R.; Larring, Y. Hydrogen in oxides. *Dalt. Trans.* **2004**, *19*, 3012–3018. [[CrossRef](#)]
52. Fan, Z.; Li, N.; Du, P.; Yang, W.; Chen, Q. Influence of Lattice Dynamics on the Proton Transport in BaZrY-Oxide Perovskites under High Pressure. *J. Phys. Chem. C* **2020**, *124*, 22376–22382. [[CrossRef](#)]
53. Abdul Malik, L.; Mahmud, N.A.; Mohd Affandi, N.S.; Mazlan, N.W.; Zakaria, N.H.A.; Abd Malek, N.I.; Hassan, O.H.; Md Jani, A.M.; Osman, N. Effect of nickel oxide—Modified BaCe_{0.54}Zr_{0.36}Y_{0.10}O_{2.95} as composite anode on the performance of proton-conducting solid oxide fuel cell. *Int. J. Hydrogen Energy* **2021**, *46*, 5963–5974. [[CrossRef](#)]
54. Bi, L.; Fabbri, E.; Traversa, E. Solid oxide fuel cells with proton-conducting La_{0.99}Ca_{0.01}NbO₄ electrolyte. *Electrochim. Acta* **2018**, *260*, 748–754. [[CrossRef](#)]
55. Agarwal, V.; Liu, M. Electrochemical Properties of BaCe_{0.8}Gd_{0.2}O₃ Electrolyte Films Deposited on Ni-BaCe_{0.8}Gd_{0.2}O₃ Substrates. *Electrochem Soc.* **1997**, *144*, 1035. [[CrossRef](#)]
56. Yang, C.; Zhang, X.; Zhao, H.; Shen, Y.; Du, Z.; Zhang, C. Electrochemical properties of BaZr_{0.1}Ce_{0.7}Y_{0.1}Yb_{0.1}O_{3-δ}-Nd_{1.95}NiO₄ + δ composite cathode for protonic ceramic fuel cells. *Int. J. Hydrogen Energy* **2015**, *40*, 2800–2807. [[CrossRef](#)]